

# Efficiency Enhancement in SynRMs Using MTPW Control and Seven-Level NPC Inverter

Sara Elbadaoui <sup>1\*</sup>, Ahmed Abbou <sup>2</sup>, Yassine Zahraoui <sup>3</sup>, Farid Oufqir <sup>4</sup>

<sup>1,2</sup> Electrical Engineering Department, Mohammed V University in Rabat, Mohammadia School of Engineers (EMI), Rabat 765, Morocco

<sup>3</sup> Systems Engineering Laboratory, Hassania School of Public Works (EHTP), Casablanca 8108, Morocco

<sup>4</sup> Electrical Engineering Department, Sultan Moulay Slimane University, National School of Applied Sciences (ENSA), Khouribga 77, Morocco

Email: <sup>1</sup> sara.elbadaoui@research.emi.ac.ma, <sup>2</sup> abbou@emi.ac.ma, <sup>3</sup> zahraoui.yassine@ehtp.ac.ma  
<sup>4</sup> farid.oufqir@gmail.com

\* Corresponding Author

**Abstract**—Multilevel inverters have emerged as a key research focus in power electronics due to their increasing importance in renewable energy systems and rotating machinery applications. These devices produce output voltages that closely approximate sinusoidal waveforms, significantly improving signal quality. Among available topologies, the Neutral Point Clamped (NPC) inverter proves particularly suitable for such applications, especially when numerous voltage levels are required. Our study examines a Synchronous Reluctance Motor (SynRM) driven by a seven-level multilevel inverter employing Maximum Torque Per Weber (MTPW) control. This approach achieves outstanding dynamic performance by directly linking torque control to current control. The selection of control methodology depends fundamentally on how reference current values are determined. Through comprehensive MATLAB/Simulink simulations, we performed a comparative analysis of conventional inverter characteristics. The results conclusively demonstrate superior performance in response time, torque ripple reduction, and current waveform quality enhancement.

**Keywords**—Multilevel Inverter; NPC Architecture; Synchronous Reluctance Motor; MTPW Control; Current Ripple Minimization

## I. INTRODUCTION

The significance of multilevel inverters in power electronics cannot be overstated [1]. These devices constitute a major advancement in power conversion technology, providing efficient solutions for enhancing electrical energy quality and optimizing performance in diverse industrial applications. By generating multiple voltage levels, multilevel inverters produce output waveforms that closely approximate ideal sinusoidal waves, thereby minimizing harmonic distortion and improving current quality [2]–[4].

Multilevel inverters are characterized by superior energy efficiency, enabling optimized power management that is crucial for systems demanding stable and reliable power supplies. Their design inherently minimizes harmonic distortion, thereby protecting sensitive equipment and extending operational lifespans.

This versatility renders them applicable across diverse domains, from electric machine drives to energy storage systems [5], [6].

Pulse Width Modulation (PWM) is widely employed for inverter control, offering a robust and effective solution particularly suited to our application given its simplicity and compatibility with seven-level inverters. While Space Vector Modulation (SVM) provides superior voltage quality and remains an attractive alternative, its implementation requires greater computational complexity [7].

Several studies have focused on connecting multilevel inverters to motors [8], [9]. Recently, however, there has been a growing trend toward the use of SynRMs [10], [11]. These machines are more economical because they contain neither rotor windings nor permanent magnets. They also offer good energy efficiency due to the absence of rotor losses. Their simple structure makes them robust and easy to maintain. Furthermore, they allow for precise control of both speed and torque [12].

The integration of reluctance motors with multilevel inverters and MTPW control significantly enhances electric drive system efficiency. Reluctance motors exploit magnetic reluctance variations for torque generation while benefiting from precise power regulation via the MTPW method [13]. This strategy optimally allocates stator current between the  $q$ - and  $d$ -axes, simultaneously minimizing power consumption and maximizing torque output. The MTPW algorithm dynamically adjusts current and voltage parameters in response to load conditions and motor characteristics, maintaining peak energy efficiency across a wide operating range.

Recent studies demonstrate significant developments in control optimization techniques for enhancing SynRM performance [14]–[16]. SynRMs have gained increasing adoption in electric vehicle traction systems and other high-speed applications [17]–[19].



This research aims to optimize SynRM vector control performance through implementation of the MTPW technique. The study is organized along two principal research axes:

- **Seven-level NPC inverter integration:** The investigation examines the incorporation of an NPC inverter topology into the SynRM drive system, with comprehensive analysis of its impact on overall system performance.
- **MTPW control strategy analysis:** The work evaluates the effectiveness of MTPW control methodologies, demonstrating their advantages in three key areas: (a) energy efficiency optimization, (b) operational speed range extension, and (c) system robustness enhancement.

To achieve our objectives, this paper is organized as follows: Section I presents the introduction, followed by an overview of principal multilevel inverter topologies in Section II. Section III describes SynRM technology, while Section IV details the field-oriented control method. Finally, Section V analyzes the simulation results, and Section VI presents the conclusions.

## II. MAIN MULTILEVEL INVERTER TOPOLOGIES

The concept of multilevel converters can be implemented using various structures, based on the combination of power semiconductors and, in some topologies, their series connections. Their common feature lies in their ability to generate an output waveform with multiple voltage levels [20]. The switching strategy and control methods of a converter are determined by the nature of the load and the specific requirements of the application. Research [21] identifies the topologies best suited for SynRMs, including *NPC*, Flying Capacitor (*FC*), and *H-Bridge* structures [22]. The first two have the advantage of operating with single-source voltage systems.

### A. NPC Family

An *NPC* inverter is a broadly used multilevel inverter topology in industrial applications requiring high-quality output waveform. The number of components needed for an *NPC* inverter depends on the desired number of voltage levels  $N_{NPC}$  at the output. It includes  $2(N_{NPC}-1)$  switches *IGBTs* that control the current path to generate the various voltage levels,  $2(N_{NPC}-2)$  clamping diodes that direct the current to the neutral point while limiting the voltage across each switch,  $(N_{NPC}-1)$  capacitors that divide the DC bus to create and stabilize the voltage levels, and  $(N_{NPC}-2)$  neutral points that serve as intermediate references for the voltages [23], [24].

### B. FC Family

An *FC* inverter is a multilevel inverter topology widely used in industrial applications requiring high quality of the output waveform. The number of components required for an *FC* inverter depends on the number of voltage levels  $N_{FC}$  desired at the output. It includes  $2(N_{FC}-1)$  switches that control the

current path to generate the different voltage levels,  $N_{FC}-1$  floating capacitors that divide the DC bus to create and stabilize the voltage levels, and  $N_{FC}-2$  neutral points that serve as intermediate references for the voltages. The equation shows the formula for fly capacitors [25], [26]. Equation (1) shows the expression for DC-link capacitor [27]:

$$C \geq \frac{1}{4f_{inv}} \cdot \frac{I_0}{\Delta v_{pp}} \quad (1)$$

The seven-level inverter features three symmetrical legs, each containing twelve bidirectional switches arranged in series. To avoid short-circuiting the inverter DC input or disrupting the inductive load, these switches must not be activated simultaneously. Each switch is made up of a bidirectional semiconductor paired with a diode connected in reverse. For the *NPC* topology, each leg of the *NPC* inverter includes ten diodes (Fig. 1), while in the *FC* topology we find ten capacitors, which are used to create various output voltage levels for each leg. Each leg is linked to a DC power source with a battery or source of energy of  $6 \times V_{dc}$ , with all six sources being equal. This inverter is classified as seven-level because it generates seven distinct voltage levels per arm:  $\frac{V_{dc}}{2}$ ,  $\frac{V_{dc}}{4}$ ,  $\frac{V_{dc}}{6}$ ,  $0$ ,  $-\frac{V_{dc}}{6}$ ,  $-\frac{V_{dc}}{4}$ , and  $-\frac{V_{dc}}{2}$ :

$$\begin{cases} \langle \text{state 6} \rangle \Rightarrow \frac{V_{dc}}{2} \Rightarrow [1, 1, 1, 1, 1, 1, 0, 0, 0, 0, 0, 0] \\ \langle \text{state 5} \rangle \Rightarrow \frac{V_{dc}}{4} \Rightarrow [1, 1, 1, 1, 1, 0, 0, 0, 0, 0, 0, 0] \\ \langle \text{state 4} \rangle \Rightarrow \frac{V_{dc}}{6} \Rightarrow [1, 1, 1, 1, 0, 0, 0, 0, 0, 0, 0, 0] \\ \langle \text{state 3} \rangle \Rightarrow 0 \Rightarrow [1, 1, 1, 0, 0, 0, 0, 0, 0, 0, 0, 0] \\ \langle \text{state 2} \rangle \Rightarrow -\frac{V_{dc}}{6} \Rightarrow [1, 1, 0, 0, 0, 0, 0, 0, 0, 0, 0, 0] \\ \langle \text{state 1} \rangle \Rightarrow -\frac{V_{dc}}{4} \Rightarrow [1, 0, 0, 0, 0, 0, 0, 0, 0, 0, 0, 0] \\ \langle \text{state 0} \rangle \Rightarrow -\frac{V_{dc}}{2} \Rightarrow [0, 0, 0, 0, 0, 0, 0, 0, 0, 0, 0, 0] \end{cases} \quad (2)$$

Each of the three legs of the inverter can independently take the seven states 6, 5, 4, 3, 2, 1, or 0. The set of possibilities for the complete inverter amounts to 73, or 343 states [28].

### C. Switching Mode Control

The PWM control mode is still the most popular [29]. It is preferred for controlling multilevel inverters, but when more than three are used, an imbalance is implemented to the capacitors of the DC link. From the output voltages  $V_{ao}$ ,  $V_{bo}$ ,  $V_{co}$ , we define the output voltage vector by:

$$V_{out} = V_{ao}e^{j\theta} + V_{bo}e^{j\frac{2\pi}{3}} + V_{co}e^{j\frac{4\pi}{3}} = V_{\alpha} + jV_{\beta} \quad (3)$$

Depending on the inverter states, the output voltage vector could take a number of positions in the  $\alpha$ - $\beta$  plane. These positions are indicated on the switching hexagon. There are 126 discrete positions, partitioned over six hexagons, in addition to a position in the hexagon center. Some positions are generated by various redundant states. From the inner hexagon to the outer one, the positions of the vector  $V_s$  were produced respectively by one, two, three, four, five, or six redundant states.

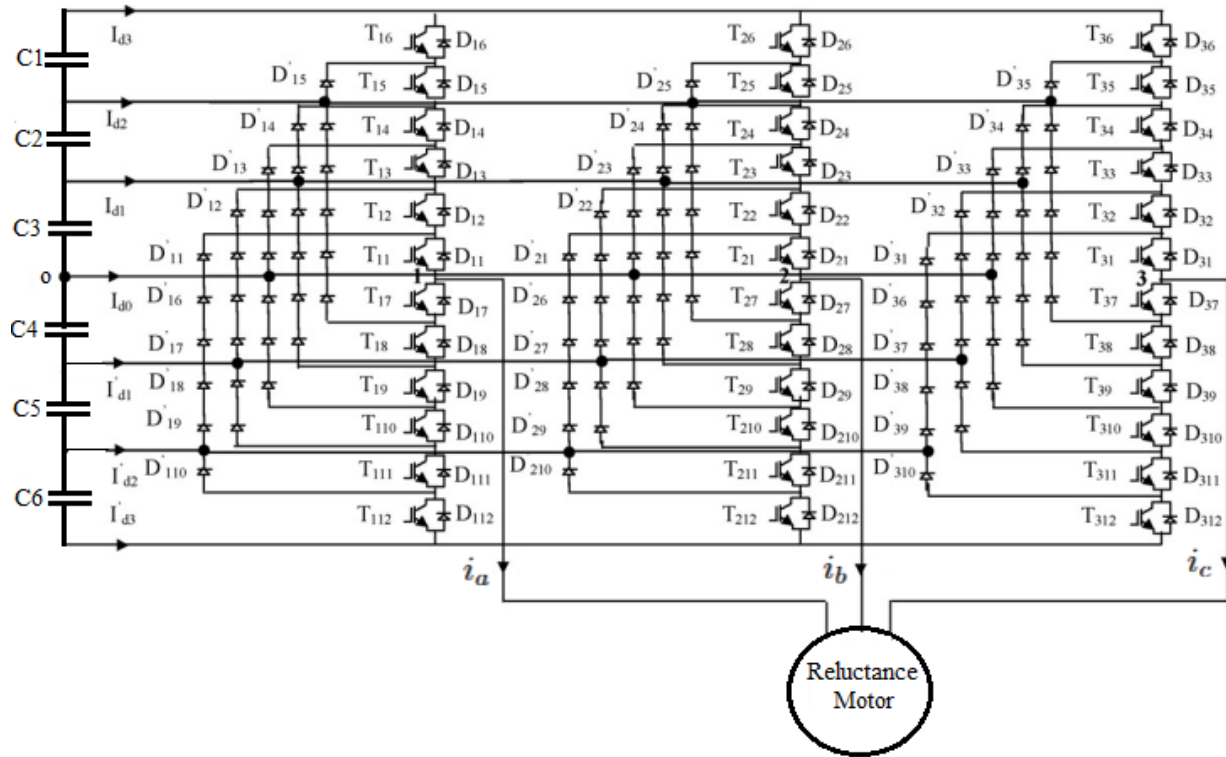


Fig. 1. Seven-level NPC inverter architecture

The position of the hexagon center, which aligns with a zero output voltage, is generated by seven redundant states. We therefore differentiate 36 positions with a single redundancy, 30 positions with two redundancies, 24 positions with three redundancies, 18 positions with four redundancies, 12 positions with five redundancies, and 6 positions with six redundancies.

The 127 positions of the output voltage vector split the vector diagram into six triangular sectors. Each sector is formed of 36 triangular regions. We thus have 216 triangular regions in the complete vector diagram. In this study, an inverter is used with DC voltage sources with PWM control to avoid this kind of capacitive voltage imbalance [30], [31].

### III. DESCRIPTION OF SYNRM

SynRM is a kind of AC motors that uses the principle of magnetic reluctance to produce rotary motion. As opposed to traditional motors, it does not contain permanent magnets or field windings, which gives its design a simple and robust structure [32]. The conventional model based on the Park transformation relies on several assumptions: the hysteresis of the magnetic circuit is minimal, the circuit is unsaturated, gap harmonics are ignored, and the distribution of magnetomotive forces in the air gap is sinusoidal. Additionally, the influence of temperature on the resistances is disregarded, which simplifies the analysis but may limit accuracy in real-

world applications [33]. The electrical equations for the SynRM in the  $d$ - $q$  reference frame are [34]:

$$\begin{bmatrix} v_{sd} \\ v_{sq} \end{bmatrix} = R_s \begin{bmatrix} i_{sd} \\ i_{sq} \end{bmatrix} + \begin{bmatrix} L_d \\ L_{sq} \end{bmatrix} \frac{d}{dt} \begin{bmatrix} i_{sd} \\ i_{sq} \end{bmatrix} + p\Omega_m \begin{bmatrix} 0 & -L_q \\ L_d & 0 \end{bmatrix} \begin{bmatrix} i_{sd} \\ i_{sq} \end{bmatrix} \quad (4)$$

where:

$i_{sd}, i_{sq}$ : stator current components.

$v_{sd}, v_{sq}$ : stator voltage components.

$L_d, L_q$ : direct and quadrature inductance.

$R_s$ : stator resistance.

$p$ : number of pole pairs.

$\Omega_m$ : mechanical speed.

The electromagnetic torque is represented as follows:

$$C_{em} = \frac{3}{2}(L_d - L_q)i_{sd}i_{sq} \quad (5)$$

The SynRM model in (4) exhibits nonlinear behavior. This nonlinearity stems from two key terms: firstly, the product of current and mechanical speed, and secondly, the product of current and its time derivative, as emphasized by [35]. The flux flowing across the windings in  $d$ - $q$  frame are expressed as:

$$\begin{cases} \phi_{sd} = L_d i_{sd} \\ \phi_{sq} = L_q i_{sq} \\ \phi_s = \sqrt{\phi_{sd}^2 + \phi_{sq}^2} \end{cases} \quad (6)$$

From (4) and (6), the direct and quadrature stator voltage is:

$$\begin{cases} v_{sd} = R_s i_{sd} + \frac{d\phi_{sd}}{dt} - p\Omega_m \phi_{sq} \\ v_{sq} = R_s i_{sq} + \frac{d\phi_{sq}}{dt} + p\Omega_m \phi_{sd} \end{cases} \quad (7)$$

The torque becomes:

$$C_{em} = p(\phi_{sd} i_{sq} - \phi_{sq} i_{sd}) \quad (8)$$

We can utilize the fundamental equations governing the dynamics of the rotor. The analysis involves considering the forces acting on the rotor and how they relate to its motion. The dynamics of the rotor can be described by Newton's second law for rotational motion:

$$J \frac{d\Omega_m}{dt} = C_{em} - C_l - f\Omega_m \quad (9)$$

where:

$f$ : the coefficient of friction;

$C_l$ : the torque of the load;

$J$ : the motor inertia.

Fig. 2 depicts the vector diagram of SynRM in steady-state.

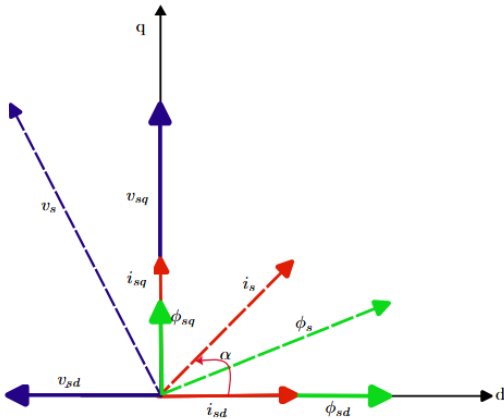


Fig. 2. Vector representation of the SynRM in steady-state

The angle of rotation of  $i_d$  is:

$$\tan \alpha = \frac{i_{sq}}{i_{sd}} \quad (10)$$

#### IV. FIELD-ORIENTED CONTROL (FOC) OF SYNRM

FOC of SynRM is a sophisticated control technique conceived to accomplish precise and efficient torque and speed control. The basic principle of FOC is to transform the stator currents from the stationary frame ( $a$ ,  $b$ ,  $c$ ) to the rotating reference frame ( $d$ ,  $q$ ), aligning the  $d$ -axis with the rotor magnetic flux and the  $q$ -axis with the torque-producing component. This transformation decouples flux-producing currents  $i_{sd}$  and torque  $i_{sq}$ , allowing independent control of each. In SynRMs,

torque is proportional to the product of  $i_{sd}$  and  $i_{sq}$ , and FOC exploits this relationship to optimize motor performance. By using two internal current control loops to regulate  $i_{sd}$  and  $i_{sq}$ , and an external speed control loop to generate the reference torque, FOC ensures precise and dynamic motor operation. Furthermore, the degree of freedom inherent in the control system allows for the optimization of other performance criteria, such as efficiency, power factor, or speed range [36], [37].

##### A. Vector Control Structure

Fig. 3 illustrates the block diagram of the SynRM vector control structure. This classical cascade structure comprises three control levels. The first level involves the current loops, which regulate the stator current  $d$ - $q$  components to preserve steady-state signals. A basic PI controller ensures zero static error and mitigates the electromotive force coupling the  $d$  and  $q$  axes. The second level determines the current set-points  $i_{sd}^*$  based on the desired torque, aiming to optimize current and voltage constraints. The final level focuses on speed control, utilizing the PI super-twisting controller as described in [38], [39].

##### B. Constant Current and Constant Current Angle

When the target speed  $\Omega_m$  is lower than the nominal speed  $\Omega_n$ , the vector control becomes an effective solution. In this operational range, the  $i_{sd}$  component is held steady, ensuring consistent performance. This approach is supported by research, such as the findings of reference [40], which validate its efficiency in applications with a lower nominal speed [41].

$$i_{sd}^* = \zeta = \frac{\phi_{smax}^*}{\sqrt{2}L_d} \quad (11)$$

where  $\zeta$  is considered constant. The maximum value of the stator flux linkage is subsequently determined on the basis of the reference value of the electromagnetic torque.

$$\phi_{smax}^* = \sqrt{\frac{4C_{em}^* L_d L_q}{3p(L_d - L_q)}} \quad (12)$$

Beyond the nominal speed, the  $i_{sd}$  component declines as the speed increases:

$$i_{sd}^* = \zeta \frac{\Omega_m}{\Omega_n} \quad (13)$$

Equation (5) yields the  $q$ -stator current reference as follows:

$$i_{sq}^* = \frac{C_{em}^*}{3p(L_d - L_q)i_{sd}^*} \quad (14)$$

##### C. Maximum Torque Per Weber (MTPW) Strategy

MTPW is designed to optimize torque production while minimizing power consumption, making it ideal for applications where energy efficiency is a priority.

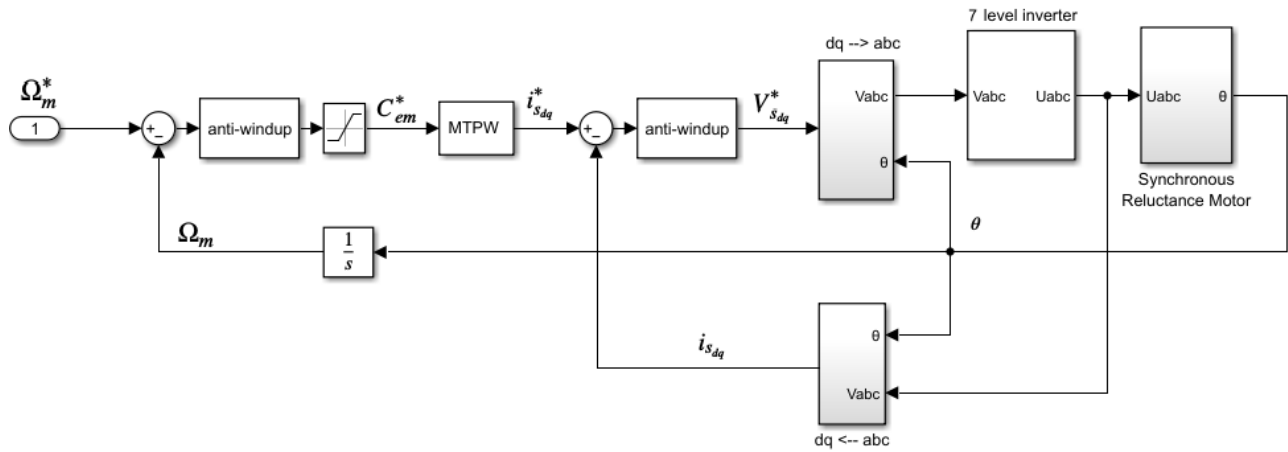


Fig. 3. Proposed vector control architecture

Unlike Maximum Torque Per Ampere (*MTPA*), which may fall short in high-speed scenarios due to voltage constraints, *MTPW* addresses this limitation by focusing on the relationship between stator voltage, flux, and rotational speed. In steady-state conditions, the stator voltage is straight proportional to the stator flux and speed. By selecting an optimal angle  $\alpha = \pm 45^\circ$ , the *MTPW* ensures efficient torque generation within voltage and speed limits, as demonstrated in [42]. This approach balances performance and energy savings, particularly in systems where voltage restrictions impact operation. The formulation of the current reference will be as follows:

$$\begin{cases} i_{sd}^* = \frac{2L_q C_{em}^*}{3pL_d - (L_d - L_q)} \\ i_{sq}^* = \frac{L_d}{L_q} i_{sd}^* \text{sign}(C_{em}^*) \end{cases} \quad (15)$$

*D. Speed Control Architecture*

Speed control of a SynRM often relies on the use of a proportional-integral (*PI*) controller. The latter minimizes the error between the set speed and the real speed of the motor by adjusting the control action. However, when the system reaches its physical limits, the windup phenomenon can occur, leading to saturation of the controller and a degraded dynamic response. The addition of an anti-windup mechanism helps mitigate this effect and improve the broad performance of the system [43], [44]. The error is sent to a gain block (with a time constant  $\tau$ ) before being fed back into the integrator. Every anti-windup controller has three tuning gains, the values of which are resolute by trial and error [45]. This method involves conducting repeated tests and adjusting each gain independently to observe its effect, as Fig. 4 shows.

To ensure good performance in reference tracking and disturbance rejection, we adopt the speed control loop schematic shown in Fig. 5. Where:

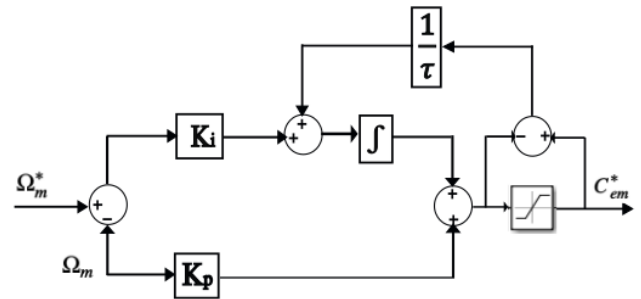


Fig. 4. Configuration of the designed anti-windup controller

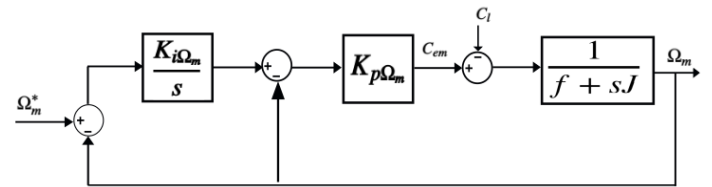


Fig. 5. Loop of speed control

$$\Omega_m(s) = \frac{1}{f + sJ} (C_{em} - C_l) \quad (16)$$

After calculation, the closed-loop transfer function is expressed as:

$$F_{f\Omega_m}(s) = \frac{1}{\frac{J}{K_{i\Omega_m} K_{p\Omega_m}} s^2 + \frac{K_{p\Omega_m} + f}{K_{i\Omega_m} K_{p\Omega_m}} s + 1} \quad (17)$$

By identification with a second order system:

$$F'(s) = \frac{1}{\frac{1}{\omega_n^2} s^2 + \frac{2\zeta}{\omega_n} s + 1} \quad (18)$$

The result is a set of identities:

$$\begin{cases} \frac{J}{K_{i\Omega_m} K_{p\Omega_m}} = \frac{1}{\omega_n^2} \\ \frac{K_{p\Omega_m} + f}{K_{i\Omega_m} K_{p\Omega_m}} = \frac{2\zeta}{\omega_n} \end{cases} \quad (19)$$

By setting  $\zeta=1$ , we can establish a connection between  $\omega_n$  and the desired speed response time  $\tau_{\Omega_m}$  which enables us to control the system dynamics. This relationship is expressed as:  $\omega_n\tau_{\Omega_m}$ . With the damping coefficient  $\zeta=1$  and a chosen response time  $\tau_{\Omega_m}=0.1s$ , we can solve for  $\omega_n$ . Once  $\omega_n$  is determined, the controller parameters can be calculated using (19) through straightforward identification, leading to the following results:

$$\begin{cases} K_{p\Omega_m} = 2J\zeta\omega_n - f \\ K_{i\Omega_m} = J\frac{\omega_n^2}{K_{p\Omega_m}} \end{cases} \quad (20)$$

### E. Sampling Period Selection

To achieve effective vector control for a SynRM, selecting a sufficiently short sampling period is essential. This is because the reference voltages computed by the control algorithm remain fixed and constant during this interval. However, in steady-state operation, the phase of the stator voltages must advance more rapidly as the machine operates at higher speeds, as highlighted by [46], [47]. For an angular velocity  $\Omega_m$ , while the sampling period  $\tau$ , the rotor of the SynRM rotates across an angle defined by the relationship:

$$\Delta\theta = \Omega_m\tau \quad (21)$$

In a steady-state condition, the phase of the reference voltages shifts solely due to the Park transformation, which is tied to the rotor's position. Consequently, it needs to be updated every  $\tau$  period. In sensorless control scenarios, this requirement can lead to challenges in computational power.

## V. SIMULATION AND RESULTS ANALYSIS

### A. Simulation Environment

The system studied in this paper was modeled in MATLAB/Simulink. It comprises a seven-level NPC inverter, implemented with IGBT semiconductors (as detailed in Section II-C), and controlled using In-Phase Disposition PWM (*PDPWM*) to supply a SynRM. The motor parameters are provided in Table I.

This method was selected for its low Total Harmonic Distortion (*THD*) and superior voltage balancing compared to alternative techniques. By maintaining all six triangular carriers in phase, *PDPWM* ensures improved harmonic distribution and reduced switching losses, making it an optimal choice for high-performance multilevel inverters.

### B. Results Analysis

The overall system design optimizes response time through the integration of an anti-windup controller, which effectively manages integrator saturation and improves transient response compared to conventional methods. Additionally, vector control ensures excellent dynamic performance, particularly during

start-up. This is demonstrated by the system's ability to compensate for load variations, resulting in a minimal speed drop of only  $1.4 \frac{rad}{s}$  at  $0.6s$  and  $1.5s$ , as well as precise reference speed tracking, as illustrated in Fig. 6. Furthermore, Fig. 7 shows that the speed error under the *MTPW* technique remains below  $6 \frac{rad}{s}$ .

TABLE I. SYNRM PARAMETERS AT RATED CONDITIONS

Parameters	Symbols	Values	Units
Power	$P$	1.1	$KW$
Speed of synchronism	$\Omega_m$	1500	$tr/min$
Torque	$C_{em}$	7	$N$
Voltage	$V$	220/380	$V$
Frequency	$f$	50	$Hz$
Stator apparent inductance in $d$ -axis	$L_d$	0.34	$H$
Stator apparent inductance in $q$ -axis	$L_q$	0.105	$H$
Moment of inertia	$J$	0.08	$N.m.s^2$

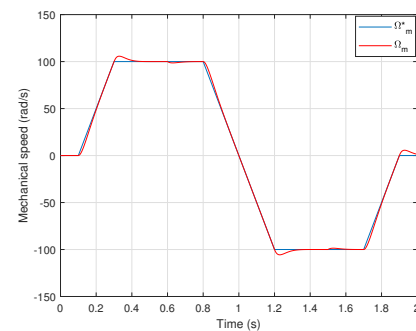


Fig. 6. Mechanical speed profile

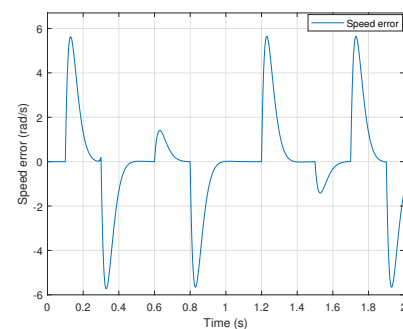


Fig. 7. Speed error

The *MTPW* control strategy produces an exceptionally smooth torque waveform, significantly reducing torque ripple. Increasing the number of inverter levels further attenuates torque fluctuations, enhancing both dynamic performance and overall torque quality (Fig. 8).

Similarly, the phase current waveform, illustrated in Fig. 9 and Fig. 10 for  $d$ - $q$  and  $a$ - $b$ - $c$  frames respectively, appears significantly smoother. The increased number of inverter levels effectively reduces phase current ripple.

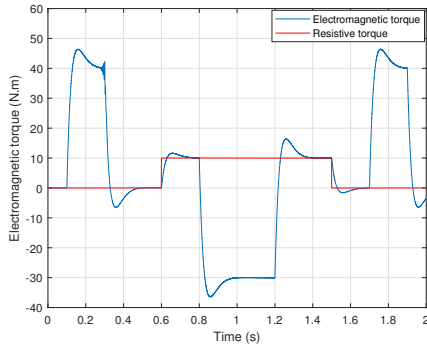


Fig. 8. Electromagnetic and resistive torque

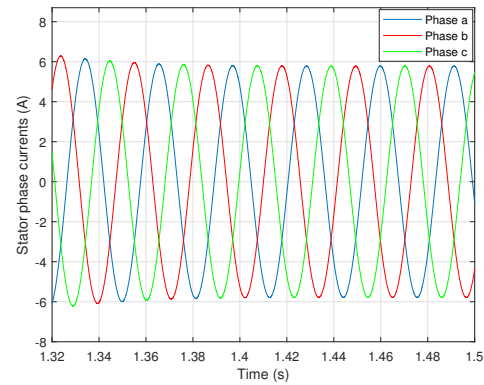


Fig. 11. Zoom on stator phase currents

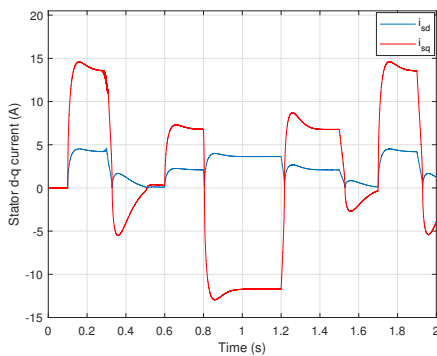


Fig. 9. Waveform of  $i_{s dq}$  currents

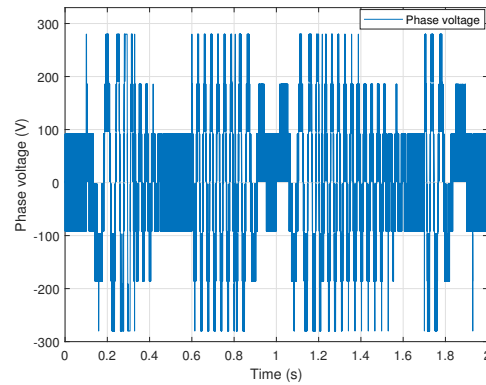


Fig. 12. Phase voltage

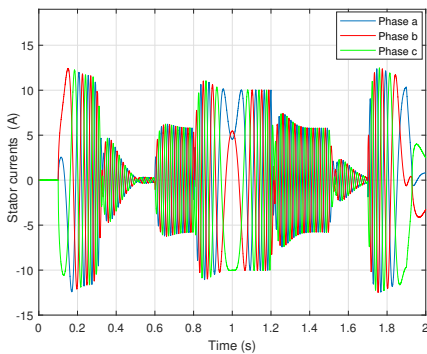


Fig. 10. Stator phase currents

The current waveforms in Fig. 11 demonstrate the three-phase sinusoidal currents over a limited interval, showing significant quality improvement compared to conventional inverters. Fig. 12 presents the output voltage levels generated by the seven-level inverter. Additionally, this architecture effectively minimizes the stator current *THD*, as evidenced in Fig. 15.

The seven voltage levels produced by the suggested *NPC* inverter are displayed in the line voltage in Fig. 13. These levels are:  $-\frac{V_{dc}}{2}$ ,  $-\frac{V_{dc}}{4}$ ,  $-\frac{V_{dc}}{6}$ ,  $0$ ,  $\frac{V_{dc}}{6}$ ,  $\frac{V_{dc}}{4}$ , and  $\frac{V_{dc}}{2}$ .

The angle required for the coordinate transformation is displayed in Fig. 14. In the vector control law, this angle is mandatory in order to transition from the bi-phase coordinates to the three-phase coordinate system and vice versa.

## VI. CONCLUSION

This research presents the modeling, identification, and simulation of a vector control strategy applied to the SynRM. The *MTPW* approach provides flexibility in managing stator currents by regulating their product based on the desired torque. When combined with a seven-level *NPC* inverter, this control method enhances performance by minimizing Joule losses and optimizing system dynamics at low speeds. Moving forward, the results of ongoing simulations aim to validate the effectiveness of this approach with other multilevel inverter topologies. The obtained *THD* value of the stator current is **37.04%**, demonstrating a significantly lower harmonic distortion level.

Potential improvements include integrating nonlinear controllers to replace the super-twisting controllers and employing an Artificial Neural Network (*ANN*) observer for mechanical speed estimation, eliminating the need for a speed sensor.

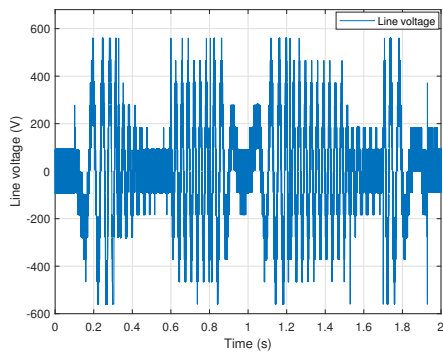


Fig. 13. Line voltage

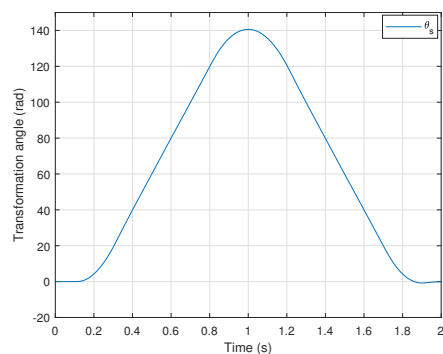


Fig. 14. Transformation angle

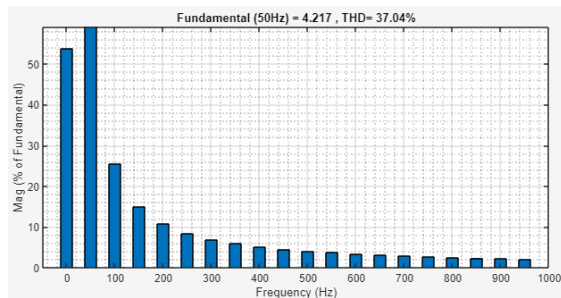


Fig. 15. Current THD rate

## REFERENCES

- [1] A. Sinha, K. Chandra Jana, and M. Kumar Das, "An inclusive review on different multi-level inverter topologies, their modulation and control strategies for a grid connected photo-voltaic system," *Solar Energy*, vol. 170, pp. 633–657, 2018, doi: 10.1016/j.solener.2018.06.001.
- [2] S. Elbadaoui, A. Abbou, A. Bouaddi, and Y. Zahraoui, "Performance study of photovoltaic generator with a three-level NPC inverter linked to the grid," *AIP Conference Proceedings*, vol. 2872, no. 1, 2023, doi: 10.1063/5.0165101.
- [3] S. Elbadaoui, A. Abbou, A. Bouaddi, R. Touleb, A. Rachid, and Y. Zahraoui, "Comparative Study Between PI and Sliding Mode Control in NPC Inverter Integrated into PV System," in *Automatic Control and Emerging Technologies*, vol. 1141, pp. 71–81, 2024, doi: 10.1007/978-981-97-0126-1\_7.
- [4] Q. Lagarde, B. Beillard, S. Mazen, M.-S. Denis, and J. Leylavernge, "Performance ratio of photovoltaic installations in France: Comparison between inverters and micro-inverters," *Journal of King Saud University - Engineering Sciences*, vol. 35, no. 8, pp. 531–538, 2023, doi: 10.1016/j.jksues.2021.11.007.
- [5] A. Bughneda, M. Salem, A. Richelli, D. Ishak, and S. Alatai, "Review of Multilevel Inverters for PV Energy System Applications," *Energies*, vol. 14, no. 6, 2021, doi: 10.3390/en14061585.
- [6] A. Poorfakhraei, M. Narimani and A. Emadi, "A Review of Multilevel Inverter Topologies in Electric Vehicles: Current Status and Future Trends," in *IEEE Open Journal of Power Electronics*, vol. 2, pp. 155–170, 2021, doi: 10.1109/OJPEL.2021.3063550.
- [7] N. A. Dobroskok and V. S. Lavrinovskiy, "Spectral Analysis of Basic Algorithms of Pulse-Width Modulation Control without Feedback in Two-Level Frequency Converters," *Russian Electrical Engineering*, vol. 92, no. 3, pp. 139–144, 2021, doi: 10.3103/S1068371221030044.
- [8] A. Poorfakhraei, M. Narimani and A. Emadi, "A Review of Multilevel Inverter Topologies in Electric Vehicles: Current Status and Future Trends," in *IEEE Open Journal of Power Electronics*, vol. 2, pp. 155–170, 2021, doi: 10.1109/OJPEL.2021.3063550.
- [9] E. Robles, M. Fernandez, J. Zaragoza, I. Aretxabaleta, I. M. De Alegria and J. Andreu, "Common-Mode Voltage Elimination in Multilevel Power Inverter-Based Motor Drive Applications," in *IEEE Access*, vol. 10, pp. 2117–2139, 2022, doi: 10.1109/ACCESS.2021.3137892.
- [10] R. V. J. M. N. V.S, S. G. N. V. Sai, and J. Rb, "Neutral-point-clamped inverter based synchronous reluctance motor drive for solar pump application," *Circuit World*, vol. 50, no. 1, pp. 120–131, 2023, doi: 10.1108/CW-05-2022-0138.
- [11] C. -K. Lin, C. A. Agustin, J. -T. Yu, Y. -S. Cheng, F. -M. Chen and Y. -S. Lai, "A Modulated Model-Free Predictive Current Control for Four-Switch Three-Phase Inverter-Fed SynRM Drive Systems," in *IEEE Access*, vol. 9, pp. 162984–162995, 2021, doi: 10.1109/ACCESS.2021.3133023.
- [12] H. Hadla and F. Santos, "Performance Comparison of Field-oriented Control, Direct Torque Control, and Model-predictive Control for SynRMs," in *Chinese Journal of Electrical Engineering*, vol. 8, no. 1, pp. 24–37, 2022, doi: 10.23919/CJEE.2022.000003.
- [13] A. Dianov, F. Tinazzi, S. Calligaro and S. Bolognani, "Review and Classification of MTPA Control Algorithms for Synchronous Motors," in *IEEE Transactions on Power Electronics*, vol. 37, no. 4, pp. 3990–4007, 2022, doi: 10.1109/TPEL.2021.3123062.
- [14] D. Igrac, A. Chowdhury, B. Štumberger, and A. Sarjaš, "Robust tracking system design for a synchronous reluctance motor – SynRM based on a new modified bat optimization algorithm," *Applied Soft Computing*, vol. 69, pp. 568–584, 2018, doi: 10.1016/j.asoc.2018.05.002.
- [15] M. N. Ibrahim, H. Rezk, M. Al-Dhaifallah and P. Sergeant, "Solar Array Fed Synchronous Reluctance Motor Driven Water Pump: An Improved Performance Under Partial Shading Conditions," in *IEEE Access*, vol. 7, pp. 77100–77115, 2019, doi: 10.1109/ACCESS.2019.2922358.
- [16] Y. Zahraoui, M. Moutchou, S. Tayane, C. Fahassa, S. Elbadaoui, and A. Ma'arif, "Synchronous Reluctance Motor Performance Improvement Using MTPA Control Strategy and Five-Level Inverter Topology," *Journal of Robotics and Control (JRC)*, vol. 3, no. 5, pp. 725–734, 2022, doi: 10.18196/jrc.v3i5.15326.
- [17] C. Chen, Z. Chen, C. Gao, J. Zhao, X. Liu, and X. Sun, "An n<sup>th</sup> Harmonic Current Suppression Method Based on the Impulse Current PWM Technique for a Multi-Phase Permanent Magnet Synchronous Motor Fed with a Current Source Inverter," *Energies*, vol. 15, no. 12, 2022, doi: 10.3390/en15124394.
- [18] E. Sangeetha and V. Ramachandran, "Different Topologies of Electrical Machines, Storage Systems, and Power Electronic Converters and Their Control for Battery Electric Vehicles—A Technical Review," *Energies*, vol. 15, no. 23, 2022, doi: 10.3390/en15238959.
- [19] M. Katona and T. Orosz, "Circular Economy Aspects of Permanent Magnet Synchronous Reluctance Machine Design for Electric Vehicle Applications: A Review," *Energies*, vol. 17, no. 6, 2024, doi: 10.3390/en17061408.
- [20] C. Gan, J. Wu, Y. Hu, S. Yang, W. Cao and J. M. Guerrero, "New Integrated Multilevel Converter for Switched Reluctance Motor Drives in Plug-in Hybrid Electric Vehicles With Flexible Energy Conversion," in *IEEE Transactions on Power Electronics*, vol. 32, no. 5, pp. 3754–3766, 2017, doi: 10.1109/TPEL.2016.2583467.

- [21] M. Deepak, G. Janaki, and C. Bharatiraja, "Power electronic converter topologies for switched reluctance motor towards torque ripple analysis," *Materialstoday: Proceedings*, vol. 52, pp. 1657–1665, 2022, doi: 10.1016/j.matpr.2021.11.284.
- [22] E. -S. Jun, M. H. Nguyen and S. -S. Kwak, "Model Predictive Control Method With NP Voltage Balance by Offset Voltage Injection for Three-Phase Three-Level NPC Inverter," in *IEEE Access*, vol. 8, pp. 172175-172195, 2020, doi: 10.1109/ACCESS.2020.3024634.
- [23] A. Balal, S. Dinkhah, F. Shahabi, M. Herrera, and Y. L. Chuang, "A Review on Multilevel Inverter Topologies," *Emerging Science Journal*, vol. 6, no. 1, pp. 185–200, 2022, doi: 10.28991/ESJ-2022-06-01-014.
- [24] S. Ozdemir, N. Altin, I. Sefa, Z. Zhang, and H. Komurcugil, "Super twisting sliding mode control of three-phase grid-tied neutral point clamped inverters," *ISA Transactions*, vol. 125, pp. 547–559, 2022, doi: 10.1016/j.isatra.2021.06.034.
- [25] Y. Ye, G. Zhang, J. Huang, S. Chen and X. Wang, "Comparative Analysis of Hybrid NPP and NPC Seven-Level Inverter With Switched-Capacitor," in *IEEE Access*, vol. 9, pp. 85852-85863, 2021, doi: 10.1109/ACCESS.2021.3088939.
- [26] J. Pribadi, D. D. Le and D. -C. Lee, "Novel Control Scheme for Five-Level Hybrid Flying-Capacitor Inverters Without DC-Link Balancing Circuits," in *IEEE Transactions on Power Electronics*, vol. 37, no. 7, pp. 8133-8145, 2022, doi: 10.1109/TPEL.2022.3149305.
- [27] M. Vujacic, M. Hammami, M. Srndovic, and G. Grandi, "Analysis of dc-Link Voltage Switching Ripple in Three-Phase PWM Inverters," *Energies*, vol. 11, no. 2, 2018, doi: 10.3390/en11020471.
- [28] R. d. B. Cardoso, E. R. C. da Silva, L. R. Limongi and A. E. L. d. Costa, "A Seven-Level Inverter With Natural Balance and Boosting Capability," in *IEEE Transactions on Industry Applications*, vol. 59, no. 1, pp. 925-937, 2023, doi: 10.1109/TIA.2022.3205882.
- [29] V. Jayakumar, B. Chokkalingam and J. L. Munda, "Performance Analysis of Multi-Carrier PWM and Space Vector Modulation Techniques for Five-Phase Three-Level Neutral Point Clamped Inverter," in *IEEE Access*, vol. 10, pp. 34883-34906, 2022, doi: 10.1109/ACCESS.2022.3162616.
- [30] J. Lara, L. Masisi, C. Hernandez, M. A. Arjona, and A. Chandra, "Novel Single-Phase Grid-Tied NPC Five-Level Converter with an Inherent DC-Link Voltage Balancing Strategy for Power Quality Improvement," *Energies*, vol. 14, no. 9, 2021, doi: 10.3390/en14092644.
- [31] H. Cheng, Z. Zhao, C. Wang, W. Yuan and J. Hao, "A Novel DC-Link Capacitor Voltage Balance Control Based on Coordination of Rectifier-Inverter Stage in a Modified Unidirectional Five-Level Converter for AC Motor Drives," in *IEEE Journal of Emerging and Selected Topics in Power Electronics*, vol. 11, no. 5, pp. 5156-5168, 2023, doi: 10.1109/JESTPE.2023.3300528.
- [32] A. Credo, M. Villani, G. Fabri and M. Popescu, "Adoption of the Synchronous Reluctance Motor in Electric Vehicles: A Focus on the Flux Weakening Capability," in *IEEE Transactions on Transportation Electrification*, vol. 9, no. 1, pp. 805-818, 2023, doi: 10.1109/TTE.2022.3204435.
- [33] C. Gan, J. Wu, Q. Sun, W. Kong, H. Li and Y. Hu, "A Review on Machine Topologies and Control Techniques for Low-Noise Switched Reluctance Motors in Electric Vehicle Applications," in *IEEE Access*, vol. 6, pp. 31430-31443, 2018, doi: 10.1109/ACCESS.2018.2837111.
- [34] C. Li, G. Wang, G. Zhang, N. Zhao and D. Xu, "Review of parameter identification and sensorless control methods for synchronous reluctance machines," in *Chinese Journal of Electrical Engineering*, vol. 6, no. 2, pp. 7-18, 2020, doi: 10.23919/CJEE.2020.000007.
- [35] Y. Zahraoui, M. Moutchou, and S. Tayane, "Vector control strategies for synchronous reluctance motor: constant current control, MTPA, MTPW and MPFC," *International Journal of Modelling, Identification and Control*, vol. 43, no. 2, pp. 154–165, 2023, doi: 10.1504/IJMIC.2023.132607.
- [36] Z. Touati, I. Mahmoud and A. Khedher, "Torque Ripple Minimization Approach of a 3-phase Switched Reluctance Motor," *2021 18th International Multi-Conference on Systems, Signals & Devices (SSD)*, pp. 533-538, 2021, doi: 10.1109/SSD52085.2021.9429463.
- [37] B. Selma, E. Bounadja, B. Belmadani, and B. Selma, "Improving dynamic response and stability of three-phase synchronous reluctance machines with a novel higher-order field-oriented sliding mode control," *International Journal of Dynamics and Control*, vol. 12, pp. 2958–2967, 2024, doi: 10.1007/s40435-024-01389-5.
- [38] S. Dwivedi, S. M. Tripathi and S. K. Sinha, "Review on Control Strategies of Permanent Magnet-Assisted Synchronous Reluctance Motor Drive," *2020 International Conference on Power Electronics & IoT Applications in Renewable Energy and its Control (PARC)*, pp. 124-128, 2020, doi: 10.1109/PARC49193.2020.236570.
- [39] Y. Zahraoui, M. Moutchou, S. Tayane, and S. Elbadaoui, "Investigation of Different Speed Controllers to Improve the Performance of Vector-Controlled Synchronous Reluctance Motor," in *Smart Applications and Data Analysis*, vol. 1677, pp. 129–143, 2022, doi: 10.1007/978-3-031-20490-6\_11.
- [40] G. Fang, F. P. Scalcon, D. Xiao, R. P. Vieira, H. A. Gründling and A. Emadi, "Advanced Control of Switched Reluctance Motors (SRMs): A Review on Current Regulation, Torque Control and Vibration Suppression," in *IEEE Open Journal of the Industrial Electronics Society*, vol. 2, pp. 280-301, 2021, doi: 10.1109/OJIES.2021.3076807.
- [41] F. -J. Lin, S. -G. Chen, M. -S. Huang, C. -H. Liang and C. -H. Liao, "Adaptive Complementary Sliding Mode Control for Synchronous Reluctance Motor With Direct-Axis Current Control," in *IEEE Transactions on Industrial Electronics*, vol. 69, no. 1, pp. 141-150, 2022, doi: 10.1109/TIE.2021.3050373.
- [42] S. Jin *et al.*, "Maximum torque per ampere control of permanent magnet/reluctance hybrid rotor dual stator synchronous motor," *IET Electric Power Applications*, vol. 18, no. 9, pp. 1021–1032, 2024, doi: 10.1049/elp2.12453.
- [43] S. -G. Chen, F. -J. Lin, C. -H. Liang and C. -H. Liao, "Development of FW and MTPV Control for SynRM via Feedforward Voltage Angle Control," in *IEEE/ASME Transactions on Mechatronics*, vol. 26, no. 6, pp. 3254-3264, 2021, doi: 10.1109/TMECH.2021.3056745.
- [44] M. A. A. Murad, M. Liu and F. Milano, "Modeling and Simulation of Variable Limits on Conditional Anti-Windup PI Controllers for VSC-Based Devices," in *IEEE Transactions on Circuits and Systems I: Regular Papers*, vol. 68, no. 7, pp. 3079-3088, 2021, doi: 10.1109/TCSI.2021.3073103.
- [45] E. Kiliç, "Deep Reinforcement Learning-Based Controller for Field-Oriented Control of SynRM," in *IEEE Access*, vol. 13, pp. 2855-2861, 2025, doi: 10.1109/ACCESS.2024.3524156.
- [46] F. -J. Lin, M. -S. Huang, S. -G. Chen and C. -W. Hsu, "Intelligent Maximum Torque per Ampere Tracking Control of Synchronous Reluctance Motor Using Recurrent Legendre Fuzzy Neural Network," in *IEEE Transactions on Power Electronics*, vol. 34, no. 12, pp. 12080-12094, 2019, doi: 10.1109/TPEL.2019.2906664.
- [47] A. Varatharajan, G. Pellegrino and E. Armando, "Sensorless Synchronous Reluctance Motor Drives: Auxiliary Flux-Based Position Observer," in *IEEE Journal of Emerging and Selected Topics in Power Electronics*, vol. 9, no. 4, pp. 4330-4339, 2021, doi: 10.1109/JESTPE.2020.3019568.